

On the Surface Heating of Synchronously-Spinning Short-Period Jovian Planets

Andreas Burkert

Max-Planck-Institut für Astronomie, Heidelberg, Germany

and

University Observatory Munich, Scheinerstr. 1, D-81679 Munich, Germany

Douglas N. C. Lin

UCO/Lick Observatory, University of California, Santa Cruz, CA 95064, U.S.A.

Peter H. Bodenheimer

UCO/Lick Observatory, University of California, Santa Cruz, CA 95064, U.S.A.

Chris A. Jones

Department of Mathematical Sciences, Exeter University, Exeter, UK

Harold W. Yorke

Jet Propulsion Laboratory, California Institute of Technology, Pasadena, CA 91109, U.S.A.

October 29, 2018

ABSTRACT

We consider the atmospheric flow on short-period extra-solar planets through two-dimensional numerical simulations of hydrodynamics with radiation transfer. The observed low eccentricity of these planets indicates that tidal dissipation within them has been effective in circularizing their orbits and synchronizing their spins. Consequently, one side of these planets (the day side) is always exposed to the irradiation from the host star, whereas the other (the night side) is always in shadow. The temperature of the day side is determined by the equilibrium which the planetary atmosphere establishes with the stellar radiation. For planets around solar-type stars with periods less than 7 days, the flux of stellar irradiation exceeds that released from their Kelvin-Helmholtz contraction by several orders of magnitude. A fraction of the thermal energy deposited on the day side is advected to the night side by a current. We show that the radiation transfer and the night-side temperature distribution in a planet's atmosphere are sensitive functions of its opacity. If the atmosphere contains grains with an abundance and size distribution comparable to that of the interstellar medium, only shallow heating occurs on the day side, whereas the heat flux carried by the circulation does not effectively heat the night side, which cools well below the day side. The temperature difference affects the spectroscopic signature of these planets. However, the temperature difference decreases as the abundance of grains in the atmosphere is reduced. This effect occurs because if the grains are depleted,

the stellar radiative flux penetrates more deeply into the atmosphere on the day side, and the higher-density atmospheric circulation carries a larger flux of heat over to the night side. A simple analytic model of the dissipation of the circulation flow and associated kinetic heating is also considered. This heating effect occurs mostly near the photosphere, not deep enough to significantly affect the size of planets. The depth of the energy deposition increases as the abundance of grains is reduced. Finally, we show that the surface irradiation suppresses convection near the photospheric region on the day side. But, in some cases, depending on the opacity, convection zones are present near the surface on the night side. This structural modification may influence the response and dissipation of tidal disturbances and alter the circularization and synchronization time scales.

1. Introduction

One of the surprising findings in the search for extra-solar planets was the discovery of short-period planets (Mayor & Queloz 1995). Tidal dissipation within the envelopes of planets in close proximity to their host stars would induce them to spin synchronously with their orbital frequency if their tidal dissipation function is comparable to that of Jupiter (Yoder & Peale 1981). Consequently, one side (the day side) of these planets would be continuously heated by the intense stellar radiation while the other side (the night side) would be permanently in shadow.

Besides its importance for the cooling of the planet, the temperature distribution at the photosphere as a function of location on the planet determines its luminosity as a function of orbital phase. This property is especially interesting with regard to the direct detectability of planets close to their stars. It may also significantly modify the spectroscopic signatures of these planets (Sudarsky, Burrows, & Pinto 2000; Seager & Sasselov 2000; Brown 2001) from those computed under the assumption of uniform surface temperature. The key issue to be addressed in this paper is the photospheric temperature distribution around the surface of a close-in giant planet and its dependence on the opacity in the planet's atmosphere.

The response of the planetary atmosphere to the source of intense stellar irradiation is important for determining other observable properties of extrasolar planets. For example, the planet around HD 209458 has been detected through transit observations (Charbonneau et al. 2000; Henry et al. 2000). The observationally inferred size of this planet appears to be 1.35 to 1.42 times Jupiter's radius R_J (Brown et al. 2001; Cody & Sasselov 2002). This relatively large size of the planet is not consistent with that expected from the evolutionary track of a gaseous giant planet with the appropriate mass. Bodenheimer, Laughlin, & Lin (2003) and Baraffe et al. (2003) find that the model radius is only about 1.1 R_J at the estimated age of HD 209458. It has been suggested that heating of the outer layers by stellar irradiation, which reduces the temperature gradient and the radiative flux in those layers, could significantly slow down the Kelvin-Helmholtz contraction of the planet and explain the large size (Burrows et al. 2000). However, even though

the stellar flux onto the planet’s surface is 5 orders of magnitude larger than that released by the gravitational contraction and cooling of its envelope, this heating effect alone increases the radius of the planet by about 10%, not by 40% as observed (Guillot & Showman 2002). An additional energy source, beyond simple stellar irradiation, contraction, and internal cooling, is needed.

A possible energy source is tidal dissipation within the planetary envelope (Bodenheimer, Lin, & Mardling 2001), caused by the circularization of the orbit. The tidal heating scenario can be tested observationally because it requires a small but non-zero eccentricity for the planet ($e \approx .03$) which needs to be induced by another hypothetical planet (Bodenheimer et al. 2001). While current observations suggest that both of these requirements could be satisfied (Bodenheimer et al. 2003), the data are not sufficiently accurate to reach any firm conclusions.

An alternative source is the kinetic heating induced by the dissipation of the gas flow in the atmosphere which occurs because of the pressure gradient between the day and night sides (Guillot & Showman 2002). In order to account for the observed size of the planet, conversion of only 1% of the incident radiative flux may be needed, provided that the dissipation of induced kinetic energy into heat occurs at sufficiently deep layers (tens to 100 bars). Showman & Guillot (2002) suggest that the Coriolis force associated with a synchronously spinning planet may induce the circulation to penetrate that far into the planet’s interior and that dissipation could occur through, for example, Kelvin-Helmholtz instability. A follow-up analysis suggests that this effect may be limited (Jones & Lin 2003). The kinetic heating scenario requires a demonstration, which has not been carried out yet, that there exists a sufficient dissipation mechanism. It would depend on the details of the circulation flow in the atmosphere. In this paper we analyze that flow and suggest a simple alternative model for kinetic heating: viscous heating arising as a consequence of shear flows that develop in an atmosphere. We consider the question of whether that heating is sufficient to result in expansion of the planet.

The three-dimensional numerical simulation presented by Showman & Guillot (2002) was designed to strengthen the case for a dissipation mechanism in the deeper layers of the atmosphere. Using approximate local heating and cooling functions, they show that the kinetic energy flux transported downward over the 100 bar surface, induced by the differential heating from the star, amounts to about 1% of the absorbed stellar flux. It is plausible that this energy is dissipated at the deeper layers by, for example, the Kelvin-Helmholtz instability, but it has not been shown how efficient this mechanism is. In the same paper the authors estimate the day-night temperature difference (their equation 11):

$$\frac{\Delta T_{dn}}{\Delta T_{rad}} \sim 1 - \exp(-\tau_{zonal}/\tau_{rad}), \quad (1)$$

where ΔT_{rad} is the difference in radiative equilibrium temperature between the day side and the night side, τ_{zonal} is a characteristic time for winds to advect energy from the day side to the night side, and τ_{rad} is the radiation diffusion time. This formula, with reasonable estimates for the time scales, indicates that ΔT_{dn} could be ~ 500 K near the photosphere (at ~ 1 bar) for a close-in giant planet. The value of ΔT_{dn} is thus strongly dependent on what is assumed for ΔT_{rad} . The

numerical simulations do not show such a large temperature variation simply because ΔT_{rad} was chosen to be only 100 K, leading to $\Delta T_{dn} \approx 50$ K, in reasonable agreement with equation (1). However, a tidally locked planet would be expected to have a night-side temperature of ~ 100 K from its internal cooling, and a day-side temperature of at least 1000 K. The simulations do not include radiation transport, and especially if the effect of stellar irradiation leads to flows at high optical depths, the effects of radiation diffusion could be quite important in the analysis of the kinetic energy flow in the deep envelope. In contrast, a two-zone analytic approximation by Jones & Lin (2003) suggests, for a standard grain opacity, a more substantial (~ 500 K) mean temperature difference between the day and night sides of the planet.

Cho et al. (2003) perform a two-dimensional hydrodynamic calculation of the flows across the surface of a close-in Jovian planet, using the shallow layer approximation to integrate over the vertical direction. The heating rate is parameterized and radiation transfer is not included. In the case that is presented in the paper, the mean day-to-night temperature variation is assumed to be 180 K, but the calculations show that, superimposed on this background variation, hot-spot/cold-spot pairs appear close to each pole, which circulate about the poles. The maximum temperature variation between the hot spot and the cold spot is about 300 K, but it could be larger depending on parameters. In both sets of simulations the local cooling approximation is a gross simplification which greatly affects the outcome of the flow. Since the flow is driven by the thermal properties of the atmosphere, it is clear that more detailed numerical models with improved physics are required to understand the complex, nonlinear radiation hydrodynamics. The validity of these simulations may be potentially tested by direct observations of the temperature difference between the day and night sides of short-period planets.

In the absence of any significant surface irradiation, the envelope of a mature gas giant planet is nearly fully convective. Surface irradiation modifies the radial temperature gradient and suppresses convection (Bodenheimer et al. 2001) at least in the upper regions on the day side. In the radiative regions of the planet's envelope, g modes (Ioannou & Lindzen 1993) and Hough modes (Ogilvie & Lin 2003) are dynamically excited by the host star's tidal disturbance. The amplitude and dissipation rate of the gravity and inertial waves determine the planet's Q values and circularization and synchronization time scales (Goldreich & Nicholson 1989; Lubow et al. 1997). Thus, it is also useful to evaluate the extent of the radiative zone near the planet's surface.

In this paper we carry out two-dimensional hydrodynamic simulations, incorporating a flux-limited diffusion treatment of radiation transport, of the flow pattern in the envelope of a synchronously spinning extra-solar Jupiter-like planet which is heated by a close-by star. The two dimensions are the depth and the azimuthal position on the surface. The quantity ΔT_{rad} is assumed to have the realistic value of 1100 K, but there is no built-in assumption regarding ΔT_{dn} . For computational simplicity we first consider the case in which the effect of rotation is limited. The spin period of a synchronously rotating close-in planet is an order of magnitude longer than that of Jupiter or Saturn. The Rossby radius v/Ω where v is a typical flow velocity (a few km s^{-1}) and Ω is the planetary angular frequency, is therefore a few times larger than the radius of the

planet so the Coriolis effect will not be dominant, but it may be of some importance. We therefore plan to consider the effect of rotation in a future investigation, but focus in this paper only on the influence of radiation transport on the dynamical structure of the planet’s atmosphere.

In §2, we briefly recapitulate the basic equations for mass, momentum, and heat transfer and describe a 2-D numerical radiative hydrodynamic scheme with which we compute the flow and structure in the planetary envelope on both the day and night side. We also explicitly state our basic assumptions and parameters and specify our initial and boundary conditions. In §3 we describe the results of our standard model, which is based on the opacity of the interstellar medium, and additional models in which we vary the opacity by 5 orders of magnitude. We show that the distribution of effective temperature over the surface is determined by the advective heat flux close to the photosphere, and that the night-side temperature depends mainly on the opacity of the photosphere on the day side. In §4 we estimate the extent of kinetic heating induced by the calculated velocity shear and an assumed viscosity. Finally, in §5 we summarize our results and discuss some of their implications.

2. The Computational Method

2.1. The basic equations

In order to investigate the gas flow in the planetary atmosphere, we have performed 2-dimensional hydrodynamical calculations adopting an Eulerian, uniform Cartesian grid code with radiation transport to treat properly stellar heating and radiative cooling. In this approximation we neglect the effect of latitudinal motion, as the rotational effect is assumed to be small. Since the vertical extent of the interesting surface region is small compared with the radius of the planet, geometrical curvature is negligibly small (see §2.2). The hydrodynamical equations are:

$$\frac{\partial \rho}{\partial t} + \vec{\nabla} \cdot (\rho \vec{v}) = 0 \quad (2)$$

$$\frac{\partial(\rho \vec{v})}{\partial t} + \vec{\nabla} \cdot (\rho \vec{v} \vec{v}) = -\vec{\nabla} P - \rho \vec{g} \quad (3)$$

$$\frac{\partial(\rho e)}{\partial t} + \vec{\nabla} \cdot (\rho e \vec{v}) + P \vec{\nabla} \cdot \vec{v} = -\vec{\nabla} \cdot \vec{F}, \quad (4)$$

where ρ , e , P and \vec{v} are the gas density, internal energy per unit mass, pressure and velocity, respectively. In the atmosphere the acceleration of gravity \vec{g} is assumed to be constant. The radiative flux \vec{F} is calculated according to flux-limited radiative diffusion

$$\vec{F} = -\frac{c\lambda}{\kappa_R \rho} \vec{\nabla} u, \quad (5)$$

where c is the speed of light, λ is the flux limiter, u is the black-body radiation energy density $u = aT^4$, where a is the radiation density constant, and κ_R is the Rosseland mean opacity. The

flux limiter is approximated according to the procedure of Levermore & Pomraning (1981):

$$\lambda = \frac{2 + R}{6 + 3R + R^2}, \quad (6)$$

where R is the ratio of the mean free path of a photon to the scale height of the radiation energy density:

$$R = \frac{|\nabla u|}{\kappa_R \rho u}. \quad (7)$$

Note that in the optically thick limit $R \rightarrow 0$ and equation (5) reduces to the normal diffusion equation for stellar interiors, and in the optically thin limit it reduces to the free-streaming solution $|F| \rightarrow cu$.

The main sources of opacity in the atmosphere of the planet, which ranges typically from 100 K to 1500 K in temperature, are ice-coated silicate grains at low T, and grains composed of silicates, amorphous carbon, and iron at temperatures above the ice evaporation temperature which is of order 170 K. The Rosseland mean opacities are taken from Pollack, McKay, & Christofferson (1985) and Alexander & Ferguson (1994), who assumed an interstellar size distribution and solar metallicity for the grains. Because 1) the size distribution in the planet's atmosphere can be different from that in the interstellar medium, 2) the grains in the upper atmosphere can be depleted due to their sedimentation to layers where they can evaporate, and 3) the planetary envelope may be enriched in heavy elements by an order of magnitude relative to their host stars, we also considered models in which the grain opacity is arbitrarily reduced or increased from the standard values by a factor of f_κ in the range of $10^{-3} - 10^2$. The high- f_κ values represent grain-enriched atmospheres whereas the low- f_κ values represent grain depletion.

2.2. The numerical method

The full computational region consists of a rectangular area with size $x_{max} \times (y_{max} - y_{min})$ and $NX \times NY$ grid cells, equally spaced in both directions. The x and y coordinates represent the azimuthal and radial directions, respectively. The point y_{min} corresponds to the base of the atmosphere, and y_{max} represents the outer edge of the grid, which is well above the level of optical depth $\tau = 1$. The x direction corresponds to a strip around the circumference of the planet, with $x_{min} = 0$ at the sub-stellar point and $x_{max} = \pi \cdot y_{min}$, 180° away on the cold side of the planet. Since the depth of the atmosphere, $(y_{max} - y_{min})$, is very small compared with x_{max} , the effects of curvature are negligible. In a few cases we tested the assumption of semi-cylindrical symmetry by using an x-grid extending the full 360° around the planet. For the non-rotating cases presented here, we found no significant signs of symmetry breaking. The set of differential equations is integrated by means of an explicit finite difference scheme with operator splitting as described by Burkert & Bodenheimer (1993, 1996). The advection terms are treated using the second-order monotonic transport scheme proposed by van Leer (1977). An artificial viscosity of the type as described by Colella & Woodward (1984) is added in order to suppress numerical instabilities.

The time rate of change of internal energy caused by radiation transport is treated in a separate radiation substep, which is carried out implicitly. The two-dimensional diffusion equation is solved iteratively using the alternating-direction implicit technique (Press et al. 1992). The radiation transport module is very similar to that used in protostellar collapse simulations by Yorke & Bodenheimer (1999).

The boundary conditions for the hydrodynamics are as follows: at each of the four boundaries the perpendicular component of the velocity is set to zero, as are the gradients, perpendicular to the surface, of the density, internal energy, and the velocity component parallel to the surface. The boundary condition for the radiation transfer at the inner boundary of the atmosphere ($y = y_{min}$) is a constant temperature (in time and as a function of x). The outer boundary condition is based on the assumption that a mature planet sufficiently close to the star rotates synchronously with its orbital motion (assumed circular). The side facing the star is heated to a temperature of $T_{equ} \cdot (\cos \theta)^{1/4}$, where θ is the angle between the directions of the host star and the normal to the surface and T_{equ} is the equilibrium temperature of the planetary surface in the radiation field of the star. At angles where this temperature falls below 100 K, which includes the entire night side of the planet, it is reset to 100 K, roughly the value expected from the internal cooling of an isolated planet. This nominal temperature on the night side corresponds to a very low-density upper atmosphere, where the optical depth falls well below unity, and its precise value does not affect the solution as long as it is low compared to the temperature on the day side.

2.3. Initial conditions

The standard model is motivated by the observations of the transiting planet HD 209458b. The model planet has solar composition, no rock/ice core, a mass of 0.63 Jupiter masses (M_J), and an outer radius (R_p) of 1.2 Jupiter radii (R_J). It is the end result, at a time of 4.1 Gyr, of an evolutionary calculation starting at a radius of 2 R_J for a spherically symmetric planet assumed to be in orbit at 0.046 AU from a solar-type star (model B1 of Bodenheimer et al. 2001). The outer region, down to a density of 0.1 g cm^{-3} or 88.5% of the outer radius, is radiative in the spherical model. The grain opacities are the same as those used for the two-dimensional calculations for Case 1 (see below) and are based on the interstellar particle size distribution with solar composition. The stellar heating gives $T_{equ} = 1200 \text{ K}$.

The 2-D grid is chosen to have its lower boundary at $y_{min} = 7.95 \times 10^9 \text{ cm}$ and its upper boundary at $y_{max} = 8.35 \times 10^9 \text{ cm}$. All calculations were performed on a grid with $NX = 150$ and $NY = 50$ grid cells in the azimuthal and radial directions, respectively. The spatial resolution is therefore $\Delta y = 8 \times 10^6 \text{ cm}$ and $\Delta x = 1.6 \times 10^8 \text{ cm}$. In the spherical model y_{min} corresponds to a temperature of 1430 K and a density of $10^{-4} \text{ g cm}^{-3}$. The intrinsic luminosity of the planet, without the effects of stellar heating, is $L_p = 2.6 \times 10^{24} \text{ erg s}^{-1}$. Initially, the density and temperature in the 2-D grid, $\rho(y)$ and $T(y)$, are set to values similar to those in the one-dimensional model for each value of x . The temperature of 1430 K, as found in the spherically symmetric

calculation at y_{min} , is adopted as the inner boundary condition for the radiation transfer in all cases.

With the θ -dependent new temperature boundary condition turned on, the spherically symmetric structure is lost owing to cooling on the night side, and a gas flow between day and night side is generated. The two-dimensional calculation is evolved with an initial damping of the gas flow velocities of 1% per time step, until the configuration has adjusted to approximate hydrostatic equilibrium. Then the damping is turned off, and the model is evolved for a few 10^7 s. This computational time corresponds to several hundred times the characteristic flow time $\tau_{\text{zonal}} \approx R_p/v \approx 10^5$ s. To compare with the local cooling time scale

$$\tau_c \sim \Sigma R_g T / F, \quad (8)$$

where R_g is the gas constant, we note that the surface density above the planet's photosphere is $\Sigma_p \sim \kappa^{-1}$ (see equation 9 below). In the normal- κ (*i.e.* $f_\kappa = 1$) model the cooling time at a mature planet's photosphere is ≈ 200 s, as the relevant flux to be used in equation (8) is the radiative flux arriving from the star. In the low- κ (*i.e.* $f_\kappa = 10^{-3}$) model the cooling times are a factor of 1000 longer but still short compared to the computation time. Also, if we use the expression given for τ_{rad} (their equation 10) by Showman & Guillot (2002), the cooling time is on the order of 10^6 s or less in the physical regime we are simulating. In this case the computational time is still many times greater than the radiation cooling time.

However, if one applies equation (8) to the deeper layers of the atmosphere, where $\rho \approx 10^{-5} - 10^{-4}$ g cm $^{-3}$, and uses the intrinsic flux, one finds that $\tau_c \sim 10^{10} f_\kappa^{-1}$ s, which is longer than the physical time scales we have computed in our simulations. The deeper layers of the models in principle have not had time to reach a fully relaxed thermal equilibrium. But in fact the standard case $f_\kappa = 1$ is started from a thermally relaxed initial condition which was generated by a spherically symmetric heated 1-D model. Thus, the base of the computational domain is close to a steady state. In the cases where $f_\kappa \neq 1$ radiative equilibrium is actually not achieved in the very deep layers, but this does not affect our results for the main part of the flow, which is dominated by the upper layers which are influenced entirely by the stellar flux, 5 orders of magnitude larger than the intrinsic flux.

2.4. Computational model parameters

In the standard model (Case 1) we consider a planetary atmosphere (1) with a grain opacity which is identical to that of the interstellar medium with solar composition and (2) with an equilibrium temperature at the planet's surface of 1200 K (see Table 1). Regarding the opacity, short-period planets have masses comparable to that of Jupiter. If their composition is similar to that of Jupiter's interior (Wuchterl, Guillot, & Lissauer 2000), which is metal-enhanced compared with solar abundances, the atmospheric opacity may be larger than that adopted in the standard model. To test the limits we consider an extreme case in which the opacity is enhanced by a

factor of 100 with respect to the standard model (Case 2). Alternatively, the grains are subject to settling, coagulation, and evaporation in deeper layers, so their opacity could well be less than that used in the standard model. We consider reductions in the standard opacity by factors of 100 (Case 3) and 1000 (Case 4).

3. The effect of opacity on the atmospheric flow and the day-night temperature difference

3.1. The standard case: interstellar opacity

With an unmodified opacity the photosphere of the planet on both the day and night sides extends to $\sim 3 \times 10^8$ cm above the base of our computational domain. The first frame of Figure 1 shows the temperature distribution and the velocity field after steady state has been reached. The inner regions at the base of the computational domain are not affected by the heating and cooling of the outer layers. Their temperature distribution is independent of x . On the other hand, near the terminator ($\theta = 90^\circ$) a strong horizontal temperature gradient is established at the layers near the photosphere where the optical depth is $\tau = 2/3$ (thick solid line), owing to stellar heating on the day side and radiative cooling on the night side. This temperature gradient, in combination with a density gradient in the x -direction for a given y , induces a strong horizontal pressure gradient. In Figure 2 we plot $f_p = P/P_{\text{av}}$, where P_{av} is the pressure averaged over all values of x for a given value of y .

The pressure gradient generates a gas flow toward the night side both above and somewhat below the photosphere, transporting heat and resulting in a temperature at the photosphere on the night side of about 500 K. At the anti-stellar point ($\theta = 180^\circ$), where the circulation currents from the two hemispheres converge, a pressure ridge is established. The location of this ridge results from the hemispherical symmetry of the system, which might be broken if Coriolis forces are taken into account. This pressure ridge drives a return flow of cool gas from the night side toward the day side below the photosphere at optical depths $\tau \approx 50$. This flow generates a cool layer with $T \approx 900$ K on the day side between the externally heated outer layers ($T \approx 1200$ K) and the internally heated inner layers ($T \approx 1400$ K).

In the first panel of Figure 3 we plot the local rate of change of internal energy per unit volume caused by radiation. In order to identify the locations where heating and cooling are most efficient, we only consider regions where $\rho > 10^{-9}$ g cm⁻³ and $\tau > 10^{-2}$, where radiative flux is transported mainly by diffusion. In Figure 1 we showed that the temperature near the day-side photosphere is heated to a local maximum. Below the photosphere the envelope's temperature decreases inward as a result of the advection of cooler material from the night side in the return flow. The inward temperature gradient leads to strong radiative heating, which compensates for the advective cooling and in addition generates an expansion near the axis $\theta = 0$, which drives an upward flow. This effect completes the circulation loop in the (x, y) plane.

In the upper layers near the terminator ($\theta = 90^\circ$) warm material moves horizontally into the shadowed region and cools strongly. On the night side the intensity of this radiative heat loss is a decreasing function of the azimuthal distance from the terminator, since the horizontally moving material at angles $\theta >> 90^\circ$ has already cooled strongly. In thermal equilibrium the loss of internal energy by radiation in this region is replenished by both the advection of excess thermal energy and the compressional PdV work. In the region of the pressure ridge near $\theta = 180^\circ$, the kinetic energy that is converted to thermal energy through PdV work is in part radiated away, heating the layers above and below. But because the region is optically thick and the radiation loss is inefficient, the temperature there remains slightly higher than that in the surroundings. The corresponding pressure gradient is able to drive the return flow. In much of the grid, however, the radiative contribution is quite small, and we find that the advective energy transport and PdV work compensate each other (eq. 4).

3.2. An analytic model of the thermal current

In Table 1 we summarize some important physical values at the photosphere on the day and night side. With the standard opacity the photosphere pressure on the day side is $P_d \approx 1 \times 10^{-3}$ bar, which is consistent with the condition for hydrostatic equilibrium,

$$P_d = \frac{2g}{3\kappa_d}, \quad (9)$$

where $g = GM_p/R_p^2 \sim 10^3 \text{ cm s}^{-2}$ is the planet's gravity, M_p is its mass, R_p is its radius at $\tau = 2/3$, and $\kappa_d \approx 1 \text{ cm}^2 \text{ g}^{-1}$ is the opacity on the day side at the photosphere. The gas temperature in the outer layers on the day side is $T_d \simeq 1200 \text{ K}$ with a corresponding sound speed $c_d \approx 2.6 \times 10^5 \text{ cm s}^{-1}$. The photospheric density on the day side is then $\rho_d = P_d \mu / (R_g T_d) \approx 3 \times 10^{-8} \text{ g cm}^{-3}$ (where μ is the mean molecular weight), and the density scale height is

$$h_d = c_d^2/g \approx 6 \times 10^7 \text{ cm}. \quad (10)$$

Note that as long as the temperature is greater than 400 K, h_d is larger than the vertical grid spacing. However, for lower T the scale height is not well resolved. (The photospheric densities and temperatures in Case 2 on the night side therefore may be under-resolved.) The total thermal energy per unit area retained in this exposed layer is

$$E_h \sim \rho_d h_d c_d^2 \sim P_d h_d \sim 2c_d^2/(3\kappa_d). \quad (11)$$

When this heated layer is advected to the night side with a speed v_d , it carries an excess flux

$$F_a \sim \frac{\rho_d v_d R_g (T_d - T_n)}{\mu}. \quad (12)$$

In Case 1 $F_a \sim 2 \times 10^8 \text{ erg s}^{-1} \text{ cm}^{-2}$, which is comparable to the incident flux due to the stellar irradiation and is much larger than the radiative flux due to the planet's internal cooling,

$F_p = L_p/(4\pi R_p^2) \approx 3 \times 10^3 \text{ erg s}^{-1} \text{ cm}^{-2}$. Thus, the surface layer of the night side is primarily heated by the advective transport.

As the circulation current reaches the night side, it cools on a characteristic time scale

$$\tau_c \simeq \frac{E_h}{F_n} = \frac{E_h}{\sigma T_n^4}, \quad (13)$$

where F_n is the radiative flux on the night side and T_n is the effective temperature at the photosphere of the night side. The night side temperature is determined by the condition that

$$\tau_c \sim \tau_x = \pi R_p/(2v_d), \quad (14)$$

where τ_x is the flow crossing time scale. As long as this equality gives $T_d > T_n$, the equilibrium is expected to be established and to be self regulated, because (i) if $\tau_x > \tau_c$, the gas temperature on the night side would decline, leading to a larger pressure gradient, shorter τ_x and a longer τ_c ; or (ii) if $\tau_x < \tau_c$, the cool side would tend to heat up, thus reducing the driving pressure differential and forcing τ_x up, while τ_c decreases.

The upper left panel of Figure 4 shows the temperature at the photosphere from day side to night side for the standard model, which varies from a maximum of 1200 K to a minimum of 480 K. The upper right panel shows the x component of the flow velocity close to the photosphere as a function of x : on the night side it maintains a nearly constant value of about $3.5 \times 10^5 \text{ cm s}^{-1}$, which, as expected, is close to c_d at 1200 K.

The advection speed v_d is induced by the pressure difference between equipotential surfaces on the two sides of the planet (Showman & Guillot 2002; Jones & Lin 2003). The maximum magnitude for v_d is of the order of the sound speed on the day side c_d . However, in a thermal equilibrium with a relatively small F_p the magnitude of v_d is also limited by the condition that the *net* rate of energy that is transported from the day to the night side by advection

$$\dot{E}_a \sim \int \frac{\rho v_d R_g (T_d - T_n)}{\mu} 2\pi r dr \quad (15)$$

must not exceed the stellar energy input rate

$$\dot{E}_d \simeq \pi R_p^2 F_d \quad (16)$$

on the day side. The integral in equation (15) extends over the vertical distance corresponding to the day-night flow. Here $F_d = L_*/4\pi a^2$ is the stellar irradiation flux with L_* the luminosity of the host star and a the semimajor axis of the planet's orbit. The condition $\dot{E}_a \leq \dot{E}_d$ leads to

$$\frac{v_d}{c_d} \leq \left(\frac{3\kappa_d R_p \sigma T_d^4}{4c_d^3} \right) \left(\frac{T_d}{T_d - T_n} \right), \quad (17)$$

which for the standard case is satisfied even when $v_d = c_d$. The hot regions on the day side cool efficiently when crossing the terminator due to their low heat capacity and collapse into a dense

cold layer on the night side, where they lead to a relatively small photospheric temperature. Under certain circumstances, however, the *gross* rate of thermal energy transported from the day to the night side in the upper atmosphere

$$\dot{E}_g \sim \int \frac{\rho v_d R_g T_d}{\mu} 2\pi r dr \quad (18)$$

could be much larger than \dot{E}_d – the limits are the same as in equation (15). In this limit $T_n \approx T_d$ and the heat advected in the optically thin layer is closely balanced by that carried in a return flow well below the photosphere, resulting in little *net* heat transport per circulation.

On the night side the thermal equilibrium condition ($\tau_c \sim \tau_x$) is satisfied when

$$T_n \approx \left(\frac{4v_d c_d^2}{3\pi\kappa_d \sigma R_p} \right)^{1/4}, \quad (19)$$

which is valid if $T_n < T_d$. For the standard model $T_n \approx 490$ K, which is fairly consistent with the numerical result of 480 K (Fig. 4). Note that T_n is not affected by the night side’s opacity, because it radiates efficiently under the black-body law. This approximation is adequate provided the advective heat flux $F_g = \rho v_d R_g T_d / \mu$ is larger than the radiative flux emerging from the planet’s interior. However, for low values of κ_d the total rate of thermal energy transport that is carried by the flow is large even though $T_d - T_n$ decreases, because $\rho_d \sim 1/\kappa$. As soon as F_g becomes large compared to the radiated flux, $T_n \approx T_d$. We will test this prediction in the next section.

We now consider qualitatively the effect of stellar irradiation on the process of heat transport from the planet’s interior. Burrows et al. (2000) suggested, on the basis of a spherical model, that surface heating reduces the magnitude of the temperature gradient near the surface, deepening the surface radiative zone and decreasing the energy loss rate and contraction rate, as compared with an isolated planet. We find that the temperature on the night side can be significantly smaller than that on the day side, depending on the opacity. Thus, the temperature gradient is increased on the night side relative to the day side, increasing the radiated flow from the interior. Heated planets with high-opacity atmospheres can therefore cool and contract faster than the spherical approximation would lead one to believe, but still not as fast as unheated, isolated planets. However, in the limit where $f_\kappa \rightarrow 10^{-3}$ the temperature distribution is almost spherically symmetric (see below and eq. 19), so that the approximation of Burrows et al. (2000, 2003) would apply. Note that the enhancement of planetary size by this effect is now thought to be smaller than the work of Burrows et al. (2000) indicated (see Guillot & Showman 2002). It would be interesting in further work to calculate this effect quantitatively by combining a long-term spherically symmetric evolution with a two-dimensional atmosphere as a boundary condition. The atmosphere would have to go deep enough so that the temperature and density are practically constant with longitude and would have to be relaxed to thermal equilibrium everywhere.

3.3. Cases with modified opacities

Table 1 compares significant properties of the various numerical simulations with different opacities at the photosphere. The quantities T_n^n , ρ_n , and P_n refer to the temperature (in K), the density (in g cm^{-3}), and pressure (in bar) at the photosphere on the night side. (A superscript ‘ n ’ is added to T_n in column 2 to represent the value obtained directly from numerical simulations.) The corresponding quantities with subscript ‘ d ’ refer to the day side. The quantity κ_d refers to the Rosseland mean opacity on the day side at the photosphere, in $\text{cm}^2 \text{ g}^{-1}$, while v_{\max} is the maximum horizontal flow velocity from the day side to the night side at the photosphere, which usually occurs over a broad region on the night side. The analytically computed values (eq. 19) of the night-side temperature T_n^a for each case are also included in Table 1.

The second frame of Figure 1 shows the temperature distribution and velocity pattern for Case 2, where the opacity is increased by a scaling factor of $f_\kappa = 100$ over the standard interstellar values. This opacity enhancement relocates the photosphere, and the opacity at the day-side photosphere κ_d is increased by a factor of 50. The corresponding panel in Figure 4 shows the temperature and velocity variations across the surface near the photosphere. The result of the numerical simulation indicates $T_n^n = 230$ K. In accordance with equation (19), $T_n^a = 200$ K (see Table 1) which agrees well with the value of T_n^n . Thus, the temperature contrast between day and night sides is even larger than that in Case 1, and the horizontal flow velocities are large, as a consequence of the larger pressure gradient. Near the photosphere the maximum horizontal velocity reaches $v_{\max} \sim 5 \text{ km s}^{-1}$, which is slightly supersonic relative to c_d and highly supersonic relative to c_n . Thus, at the anti-stellar point there is a shock, which leads to enhancement of density and temperature by compressional heating. This effect is clearly visible in the velocity and temperature profiles (Fig. 4). The enhanced pressure behind the shock leads to upward and downward flows near $\theta = 180^\circ$. The downward flow feeds the return flow toward the hot side.

As would be expected from equation (9), photospheric densities and pressures are considerably smaller in Case 2 than in Case 1, since the photosphere lies at a higher level in the atmosphere (see Fig. 1). The depth of the level where the horizontal flow switches from positive to negative velocities also lies higher in Case 2. Compared to Case 1, the region where the reverse flow leads to a cold layer on the day side is larger in vertical extent and with a lower minimum temperature of $T=850$ K. Note also that in this case the reverse flow is still far below the photosphere but at a higher level than in Case 1.

The temperature and velocity variations for Case 3, in which the opacity is uniformly reduced by a factor 100 from the standard case, are illustrated in the third frames of Figures 1 and 4. The corresponding reduction in κ_d is a factor of 25. The level of the photosphere is considerably deeper than in the previous cases, and the pressures and densities are correspondingly enhanced in accordance with equation (9). The main day-to-night flow lies above the photosphere and is much broader in vertical extent than in the previous cases. The heated layer, which is denser than in Case 1, carries a large amount of thermal energy from the day to the night side. The

photospheric temperature on the day side is somewhat reduced from the standard model in Case 1, and the photosphere extends down to the cooler layer of the return flow. The reason for the lower photospheric temperature is, however, not necessarily due to cooling from the return flow, as explained below. In Cases 1 and 2 the return flow on the day side is heated by inward diffusion of radiation, while in Cases 3 and 4 the upper layer of the return flow lies in the optically thin region and is directly heated. The advective transport of heat from the day to the night sides also increases the temperature on the night side such that the temperature contrast between day and night sides is much reduced compared with the previous cases, with a higher average night-side temperature of about 850 K, in agreement with equation (19). Consequently, the horizontal flow velocities are reduced, with an average value on the night side of 1.5×10^5 cm s $^{-1}$ as compared with 3.5×10^5 cm s $^{-1}$ in the standard case.

On the night side the region where most of the radiative loss occurs is above the photosphere near the terminator (Fig. 3). But at larger values of x , because of cooling, the scale height decreases and material collapses to smaller radii. The flow toward the anti-stellar point becomes increasingly concentrated near the photosphere.

In Table 2 we tabulate the gross heat flux $F_g = \rho_d v_d R_g T_d / \mu$ at the photosphere on the day side. The magnitude of F_g is of order 10^{10} erg cm $^{-2}$ s $^{-1}$ in Case 3. For Cases 3 and 4 F_g is large compared to the radiative stellar heat flux, which is of order $F_d = 3 \times 10^8$ erg cm $^{-2}$ s $^{-1}$. The high value of F_g is balanced by the flux in the return flow in the high-density regions below the photosphere.

The trends seen in Case 3 continue in Case 4, where the opacity reduction from the standard model is by a factor 10^3 . The corresponding reduction in κ_d is a factor of 250. The temperature and velocity patterns are shown in the fourth frames of Figures 1 and 4. On the day side the photospheric pressures and densities are about a factor 10 higher than in Case 3 (see Table 1).

The main day-night flow is again above the photosphere, which now penetrates deeply into the layer of the cooler reverse flow. As the temperature in the reverse flow is almost constant, the temperature difference at the photosphere between the day and night side is practically zero. As the photosphere is actually in the return flow, the velocity there is negative with a nearly constant value of 0.2 km/s. The value of T_d is reduced to 1030 K.

In addition to the back-flow effect, there is an additional reason why there is a drop in T_d compared with the previous cases. The total incident luminosity from the stellar irradiation is $(A/2)F_*$ where $F_* = L_*/4\pi a^2$ is the stellar flux and $A/2$ is the effective area of the day side. The total radiation released from both sides of the planet is $\approx (A/2)\sigma(T_d^4 + T_n^4)$. At thermal equilibrium these two rates balance. Thus, if we define an effective temperature T_{eff} such that $F_* = \sigma T_{\text{eff}}^4 = 1200$ K in our cases, then the temperature of the photosphere at the day-side becomes

$$T_d = T_{\text{eff}} \left(\frac{1}{1 + T_n^4/T_d^4} \right)^{1/4}. \quad (20)$$

Since $T_n \sim T_d$, T_d is reduced by $2^{1/4} \sim 1.2$ compared with T_{eff} . Interestingly, the temperature in the return flow at the photosphere happens to agree with this estimate. In contrast if $T_n \ll T_d$ as in Case 2, then $T_d \approx T_{\text{eff}}$.

In Table 1 we compare the temperature obtained from our numerical simulation (T_n^n) with that obtained from our analytic approximation (T_n^a). The agreement between them is remarkable. Our results can be compared with the estimates of Showman & Guillot (2002), who assume that grains are mostly depleted in the planetary atmosphere and who adopted an equivalent opacity in their calculation that is comparable to or even lower than that which we use in Case 4. Based on a Newtonian local cooling approximation (rather than diffusion through an opaque atmosphere), they estimate the temperature difference $\Delta T_{dn} = T_d - T_n$ to be 500 K. Our results do not agree with their conclusion, since we clearly obtain $T_d \approx T_n$ in Case 4. If we use our cooling time estimate from equation (13) for τ_{rad} in equation (1), we do obtain only a 10% difference between T_d and T_n . The difference must lie in their alternate approach to the calculation of τ_{rad} . These results clearly indicate that 1) the atmospheric dynamics are driven by the radiation transfer process, and 2) the local Newtonian cooling prescriptions adopted in the previous investigations are oversimplified.

4. Energy deposition and transport

4.1. Shear and kinetic heating of interior regions

The total heating rate \dot{E}_d , as well as the gross and net advective heat fluxes near the photosphere \dot{E}_g and \dot{E}_a , are much larger than the intrinsic luminosity of a few-Gyr-old Jupiter-mass planet. The Kelvin-Helmholtz contraction and internal cooling of our standard model planet give a flux of heat loss $F_p \approx 3000 \text{ erg cm}^{-2} \text{ s}^{-1}$, which is five orders of magnitude smaller than $F_d \approx 3 \times 10^8 \text{ erg cm}^{-2} \text{ s}^{-1}$. Guillot & Showman (2002) suggest that a modest amount of dissipation of the energy associated with the advective flow, if deep enough in the atmosphere, could produce sufficient heating and mechanical work to expand the atmosphere. The circulation pattern which has been described in previous sections produces a shear, which is most important at the interface between the day-to-night flow and the return flow. Showman & Guillot (2002) suggest that a shear layer of this type could provide a kinetic heating source through the effects of Kelvin-Helmholtz instabilities. But they require that the major dissipation take place at lower levels in the atmosphere than the shear layer evident in Figure 1.

As a first approximation of this heating effect, we assume an effective viscosity ν , which leads

to a rate of energy dissipation per unit volume of

$$\dot{e}_k = \rho \nu \left(\frac{dv_x}{dy} \right)^2. \quad (21)$$

Integrating over the entire volume V of the atmosphere, the total kinetic energy dissipation is $\dot{E}_k = \int \dot{e}_k dV$ (the x - velocity gradient clearly dominates over that in y).

Although we do not include the effect of viscous drag in the momentum equation which we solved numerically, we can compute the distribution of \dot{e}_k from our results. As in typical astrophysical situations, molecular viscosity is too small to make any significant contribution. The flow near the interface layer does in fact lead to a Richardson number less than the critical value of 1/4, which would induce a shearing instability (Showman & Guillot 2002). However, modification of the stability criterion is needed from the traditional Boussinesq approximation, because both the stabilizing buoyancy effect and the destabilizing shear are modified by both heating and cooling efficiencies (Garaud & Lin 2003; Jones & Lin 2003). If the shear flow were unstable, we could determine a viscosity with an *ad hoc* α prescription (Shakura & Sunyaev 1973), in which

$$\nu = \alpha c_s h_s \simeq \alpha c_s^3 / g, \quad (22)$$

where c_s is the local magnitude of the sound speed and h_s is the local pressure scale height.

For Cases 1 and 3 we obtain the \dot{e}_k distribution shown in Figure 5 (for $\alpha = 1$). This figure shows that for this particular prescription of determining the dissipation, the kinetic dissipation rate has very little effect on the energy flow at high pressures, because the shear at lower levels in the atmosphere is small. The most intense dissipation occurs mostly on the night side in the vicinity of the shear layer.

In Figure 6 we plot the quantity $\alpha^{-1} F_k$, where F_k is defined as the total energy dissipation rate in the grid per unit surface area, integrated over all x and from the upper edge of the grid down to some cutoff pressure P . The results show that the quantity F_k saturates to a value $F_{k,\text{tot}}$ in the deeper layers, indicating that the major contributions occur at relatively low optical depth, in regions where dF_k/dy is at a maximum and the local pressure P_m (see Table 2) is in the range 10^{-3} to 0.1 bar. The total amount of energy dissipated per unit area, indicated by the horizontal parts of the curves, increases roughly as $F_{k,\text{tot}} \propto 1/\sqrt{\kappa}$.

The total integrated values of $\alpha^{-1} F_k$ (asymptotic value in the limit of high P), corresponding to the highest values on the curves in Figure 6, are shown in Table 2. These values should be compared with the incident radiation flux $F_d \approx 3 \times 10^8 \text{ erg cm}^{-2} \text{ s}^{-1}$. For the high opacity Cases 1 and 2 the integrated flux F_k can be quite significant, if α is greater than of order $10^{-2} - 1$. In the low opacity cases the integrated $F_{k,\text{tot}}$ is smaller than F_d only if $\alpha < \approx 5 \times 10^{-3}$.

If the kinetic energy associated with the shear is dissipated very close to the surface, it would be radiated without significantly modifying the planet's envelope. If, on the other hand, a significant fraction ($\sim 10^{-2}$) of the stellar irradiative flux is dissipated in a region with pressure

between 10 and 100 bar, the envelope may adjust to a new hydrostatic equilibrium by expanding its radius (Guillot & Showman 2002). From Figure 6 we find that if $\alpha \approx 10^{-2}$, more than 99% of the total incident stellar irradiative flux is dissipated at a pressure which is well below 1 bar. Little or no expansion is expected.

The results in Figure 6 also justify our neglect of the viscous effects in the numerical treatment of the momentum and the energy equations for modest values of α , because much of the energy dissipation that occurs in the optically thin zones is radiated locally. However, in the high viscosity (α) limit where

$$\dot{F}_k \geq \dot{F}_d, \quad (23)$$

the viscous momentum transfer and energy dissipation would reduce the velocity gradients until a new equilibrium is established whereby $\dot{E}_k < \dot{E}_a$. In this regard, we tabulate in Table 2 a quantity

$$f_k \equiv F_k(y_1)/\alpha F_*, \quad (24)$$

where $F_k(y_1)$ is the energy dissipation flux between y_{max} and the y -level where $P = 1$ bar, where most of the energy is dissipated. For all cases $f_k > 1$ for $\alpha = 1$. But f_k should be less than unity, which means α is required to be less than $\sim 10^{-2}$. The results in Table 2 indicate that f_k increases as the opacity drops. This dependence arises naturally since the pressure at the photosphere increases as κ_d drops. Although stellar irradiation is able reach deep down in the low-opacity Cases 3 and 4, the smaller temperature differences between the day and night sides of the planet limits the magnitude of the flow speed and therefore that of the shear.

Based on these results, it is worthwhile to further examine the effect of energy dissipation associated with the circulation by including the viscous transport and energy dissipation contributions in the governing equations. In our calculations we also neglected rotation, especially the Coriolis effect. In principle, this process can induce the circulation current to mix to a different depth. We will check the radial extent of this mixing in the future.

4.2. Heat transfer

In the absence of any significant surface irradiation the envelope of a mature gas giant planet is nearly fully convective. In our particular spherically symmetric planetary structure models the surface irradiation suppresses convection down to $\sim 0.9R_p$ (Bodenheimer et al. 2001). The results in Figure 1 indicate that the convection in the planetary envelope is suppressed at least on the day side. The extent of the radiative zone affects the planet’s structure and evolution in four ways. 1) The heat diffusion flux through the radiative zone may lead to a reduction in the planet’s cooling rate. 2) A stable thermal stratification may also suppress the onset of shearing instability associated with the circulation flow. 3) The suppression of convection may enhance the rate of grain sedimentation and modify the magnitude of the opacity. 4) The tidal disturbance can lead to g mode excitation (Lubow et al. 1997) in radiative zones, whereas Hough modes may be excited in convective zones (Ogilvie & Lin 2003).

We plot in Figure 7 the distribution of the local normalized Brunt–Väisälä frequency where $N_n^2 \equiv R_p^3 N^2 / GM_p$ for Cases 1 and 3 (with standard and reduced opacities). The magnitude is determined from

$$N^2 = \frac{1}{\rho} \frac{dp}{dr} \left(\frac{d \ln \rho}{dr} - \frac{1}{\gamma} \frac{d \ln p}{dr} \right), \quad (25)$$

where γ is the adiabatic exponent. Positive and negative values of N_n^2 represent the radiative and convective regions respectively. In both cases the day side is radiative throughout the computational domain. Note that the inner boundary condition we have adopted is matched to the radiative region deduced from the 1-D spherical calculation, which includes the effect of stellar irradiation. The magnitude of N_n^2 is maximum near the photosphere where the stellar irradiation is mostly absorbed.

On the night side the surface region becomes convective near the photosphere in Case 1. The extent of the convective region appears to be confined. Below it there is a relatively intensive radiative layer which is also confined. In Case 3 thermal energy transport by the circulation current does not alter the radiative state on the night side throughout the entire computational domain. The distribution of N_n^2 is independent of the longitude (x) in the deeper regions in Case 1. A slight longitudinal variation in N_n^2 near the inner boundary in Case 3 may be attributed to the fact that thermal equilibrium has not completely been established for this low opacity case.

The existence of a radiative surface layer supports the suggestion that g-mode oscillations may be excited just above its interface with the planet’s convective envelope and dissipated through radiative or nonlinear damping (Lubow, Tout, & Livio 1997). Outwardly propagating Hough waves may also be excited within this radiative layer and be damped in the atmosphere (Ogilvie & Lin 2003). This process may play a dominant role in driving the short-period extrasolar planets toward a state of synchronous rotation.

5. Summary and discussion

In this paper we consider the circulation arising from stellar irradiation in the atmospheres of synchronously-spinning short-period planets around nearby stars. Our results confirm early suggestions that one-sided heating can lead to circulation flow from the day to the night sides of these planets (Showman & Guillot 2002; Cho et al. 2003). This circulation current carries with it considerable thermal energy content, which provides a heating source for the planets’ night sides. At the night side of the planets where the circulation flow converges, the cool and dense gas submerges and induces a reverse flow. The returning current occurs well below the photosphere. The returning current is generally cooler than its ambient gas. Consequently, radiation diffusion into this layer is enhanced. The returning current eventually converges on the sub-stellar point where the diverging flow near the surface leads to a local reduction of density and pressure. The resurfaced current completes a circulation pattern with the excess heat transported advectively to the surface and radiated at the photosphere of both day and night sides of the planet. This flow

pattern indicates that the surface irradiation on a synchronously spinning planet may not suppress the cooling of its interior as much as suggested by Burrows et al. (2000, 2003) on the basis of a one-dimensional model. However, a more rigorous follow-up study is needed.

In contrast to previous investigations, we take into account the effect of radiative diffusion in the planetary atmosphere and envelope. We show that the night side temperature is a sensitive function of the atmospheric opacity. If the grain content in the atmosphere were comparable to that in the interstellar medium, only a shallow layer in the planetary atmosphere would be exposed to the stellar irradiation. This limited supply of heat to the night side would lead to a relatively low effective temperature there. The relatively large azimuthal temperature and pressure differential along an equipotential surface would induce the flow to become transonic. If the shear flow induced by the circulation pattern is unstable and the resultant turbulence is efficient in inducing mixing between the layers, the dissipation of energy can be modest. However, most of this energy dissipation occurs near the photosphere such that it is likely to be rapidly radiated away.

If the grains were depleted, the stellar irradiation would be able to penetrate deeply into the planet's atmosphere. The circulation current would carry much greater mass and thermal energy flux than in the standard Case 1. Since only a portion of the incident stellar thermal energy flux is reprocessed, the day-side effective temperature for the low-opacity cases is lower than that for the normal and high-opacity cases. In contrast, the night side receives the heating induced by advective circulation, so the surface temperature is relatively large. Both of these effects reduce the temperature differential between the day and night side. The reduced circulation speed implies that less energy would be dissipated. Although the photosphere extends deeply into the planet's atmosphere, the dissipation of the circulation flow would occur below the photosphere. For the reduced-opacity Cases 3 and 4, the energy release, as a consequence of this dissipation, occurs well below the surface. Our estimated rate of energy dissipation does not appear to be adequate to account for the inflation of the short-period planet around HD209458 to its presently observed value (Brown et al. 2001).

The above summary clearly indicates that the radiative properties and the dynamical structure of the atmosphere of close-in planets depend sensitively on the presence and depletion of grains. We have not considered the dynamical effect of the circulation on the grain evolution in the planetary atmosphere. A preliminary estimate suggests that the characteristic time scale of the circulation is comparable to the sedimentation time scale of relevant size grains in the planetary envelope. In a subsequent paper we shall examine the self-consistent evolution of the grains in such an atmosphere.

We also neglected the effect of rotation which introduces a Coriolis force to the flow. This effect may lead to latitudinal circulations as well as vorticity stretching. It may suppress heat flow from the equator to the poles as well as break the hemispheric longitudinal symmetry. It could also induce the circulation to penetrate farther into the planet's interior and to couple the

flow in the azimuthal and radial directions. Finally, it could lead to instabilities to enhance the dissipation of the shear associated with the circulation flow. These issues need to be examined in three dimensions with a proper treatment of the radiation transfer, a problem which will also be considered in a future study.

We wish to thank G. Novak for useful conversation and valuable comments. This work is supported by NSF and NASA through grants AST-9987417 and NCC2-5418. This work was supported in part by the European Community's Human Potential Programme under contract HPRN-CT-2002-00308,PLANETS.

TABLE 1

Case	T_n^n	T_n^a	ρ_n	P_n	κ_d	T_d	ρ_d	P_d	v_{max}
1	480	490	3×10^{-8}	6×10^{-4}	1	1200	3×10^{-8}	1.2×10^{-3}	3.5×10^5
2	230	200	3×10^{-9}	4×10^{-5}	50	1200	4×10^{-10}	2×10^{-5}	5×10^5
3	850	840	7×10^{-7}	3×10^{-2}	0.04	1100	5×10^{-7}	2×10^{-2}	1.2×10^5
4	990	960	6×10^{-6}	0.25	0.004	1050	4×10^{-6}	0.17	$< 2 \times 10^4$

TABLE 2

Case	F_g	F_d	F_n	$\alpha^{-1}F_k$	P_m	f_k
1	9×10^8	3×10^8	3×10^6	3.3×10^9	2×10^{-3}	11
2	4×10^7	3×10^8	1.6×10^5	9.6×10^8	1×10^{-3}	3.2
3	6×10^9	3×10^8	3×10^7	2.7×10^{10}	3×10^{-2}	90
4	8×10^9	3×10^8	5.4×10^7	5×10^{10}	0.1	167

REFERENCES

Alexander, D. R., & Ferguson, J. W. 1994, *ApJ*, 437, 879

Baraffe, I., Chabrier, G., Barman, T. S., Allard, F., & Hauschildt, P. H. 2003, *A&A*, 402, 701

Bodenheimer P., Laughlin, G., & Lin, D. N. C. 2003, *ApJ*, 592, 555

Bodenheimer P., Lin, D. N. C., & Mardling, R. A. 2001, *ApJ*, 548, 466

Brown, T. M. 2001, *ApJ*, 553, 1006

Brown, T. M., Charbonneau, D., Gilliland, R. L., Noyes, R. W., & Burrows, A. 2001, *ApJ*, 552, 699

Burkert, A., & Bodenheimer, P. 1993, *MNRAS*, 264, 798

Burkert, A., & Bodenheimer, P. 1996, *MNRAS*, 280, 1190

Burrows, A., Guillot, T., Hubbard, W. B., Marley, M., Saumon, D., Lunine, J. I., & Sudarsky, D. 2000, *ApJ*, 534, L97

Burrows, A., Sudarsky, D., & Hubbard, W.B. 2003, *ApJ*, 594, 545

Charbonneau, D., Brown, T. M., Latham, D. W., & Mayor, M. 2000, *ApJ*, 529, L45

Cho, J. Y.-K., Menou, K., Hansen, B. M. S., & Seager, S. 2003, *ApJ*, 587, L117

Cody, A. M., & Sasselov, D. D. 2002, *ApJ*, 569, 451

Colella, P., & Woodward, P. 1984, *J. Comput. Phys.*, 54, 174

Garaud, P., & Lin, D. N. C. 2003, *ApJ*, submitted

Goldreich, P., & Nicholson, P. D. 1989, *ApJ*, 342, 1079

Guillot, T., & Showman, A. P. 2002, *A&A*, 385, 156

Henry, G. W., Marcy, G. W., Butler, R.P., & Vogt, S.S. 2000, *ApJ*, 529, L41

Ioannou, P. J., & Lindzen, R. S. 1993, *ApJ*, 406, 252

Jones, C., & Lin, D. N. C. 2003, in preparation

Levermore, C. D., & Pomraning, G. C. 1981, *ApJ*, 248, 321

Lubow, S. H., Tout, C. A., & Livio, M. 1997, *ApJ*, 484, 866

Mayor, M., & Queloz, D. 1995, *Nature*, 378, 355

Ogilvie, G. I., & Lin, D.N.C. 2003, ApJ, submitted

Pollack, J. B., McKay, C., & Christofferson, B. 1985, Icarus, 64, 471

Press, W. H., Teukolsky, S. A., Vettering, W. T., & Flannery, B. P. 1992, Numerical Recipes: The Art of Scientific Computing (Cambridge: Cambridge Univ. Press), p. 861

Seager, S., & Sasselov, D. D. 2000, ApJ, 537, 916

Shakura, N. I., & Sunyaev, R. A. 1973, A&A, 24, 337

Showman, A. P., & Guillot, T. 2002, A&A, 385, 166

Sudarsky, D., Burrows, A., & Pinto, P. 2000, ApJ, 538, 885

van Leer, B. 1977, J. Comput. Phys., 23, 276

Wuchterl, G., Guillot, T., & Lissauer, J.J. 2000, in Protostars and Planets IV, ed V. Mannings, A. P. Boss, & S. S. Russell (Tucson: Univ. of Arizona Press), 1081

Yoder, C. F., & Peale, S. J. 1981, Icarus, 47, 1

Yorke, H. W., & Bodenheimer, P. 1999, ApJ, 525, 330

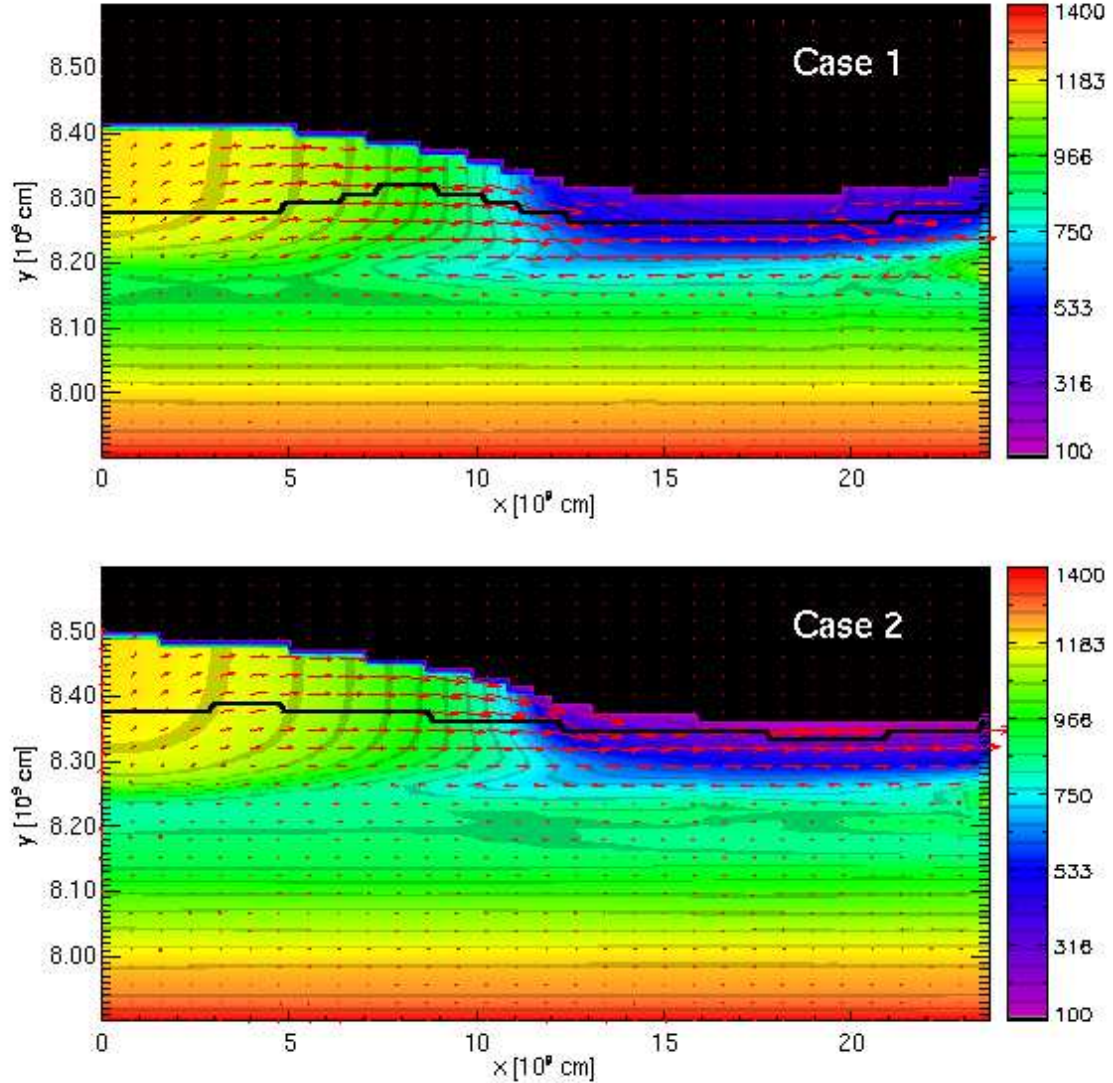


Fig. 1a.– Colors represent temperatures in the (x, y) plane for Cases 1 and 2 when they have reached steady state. Color scale runs from 1400 K (red) to 100 K (violet). The black line corresponds to the photosphere ($\tau = 2/3$). Arrows correspond to velocity vectors, with length proportional to speed and with a maximum of 3 km/s.

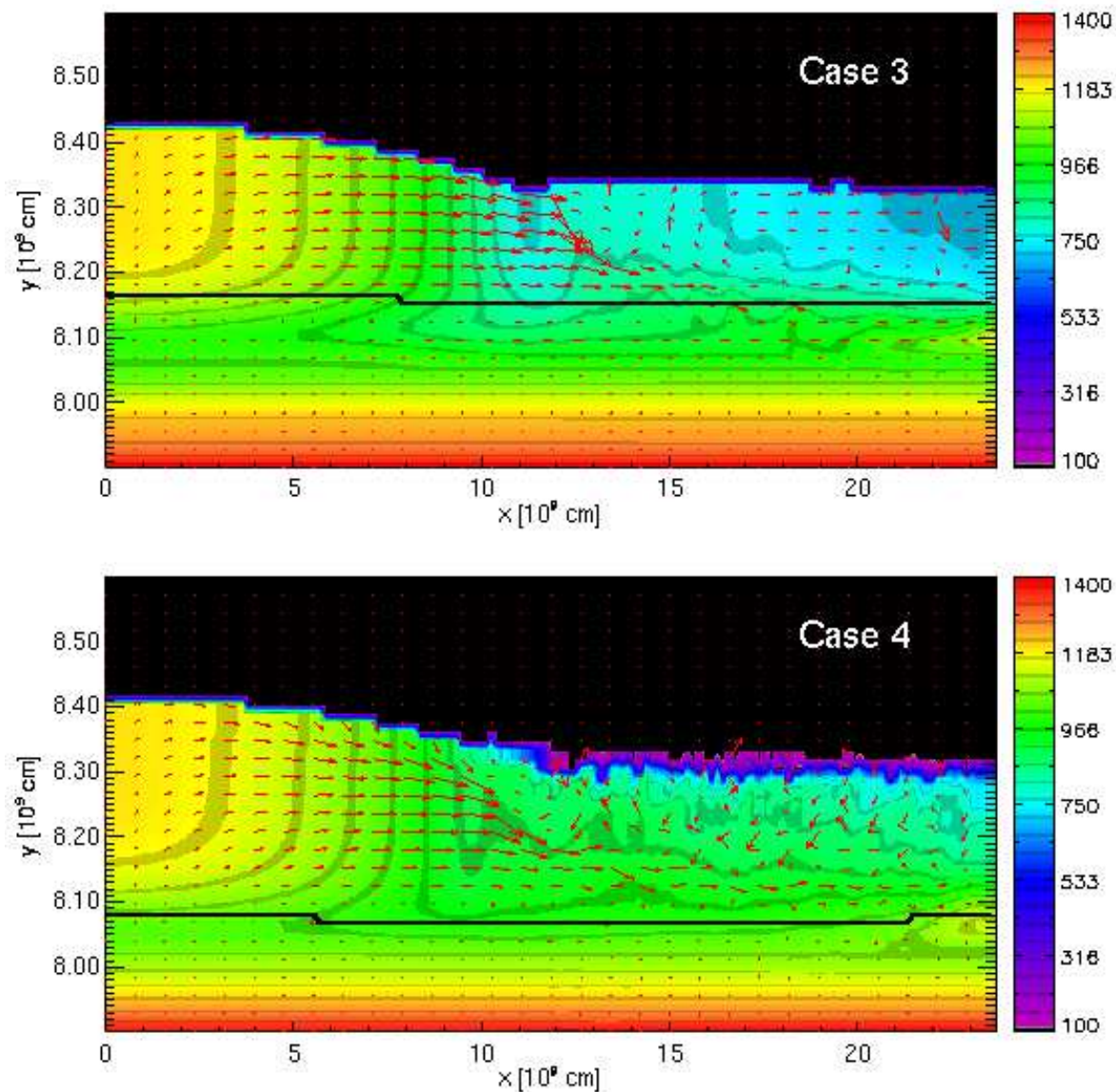


Fig. 1b.— Same as Fig. 1a except that Cases 3 and 4 are plotted.

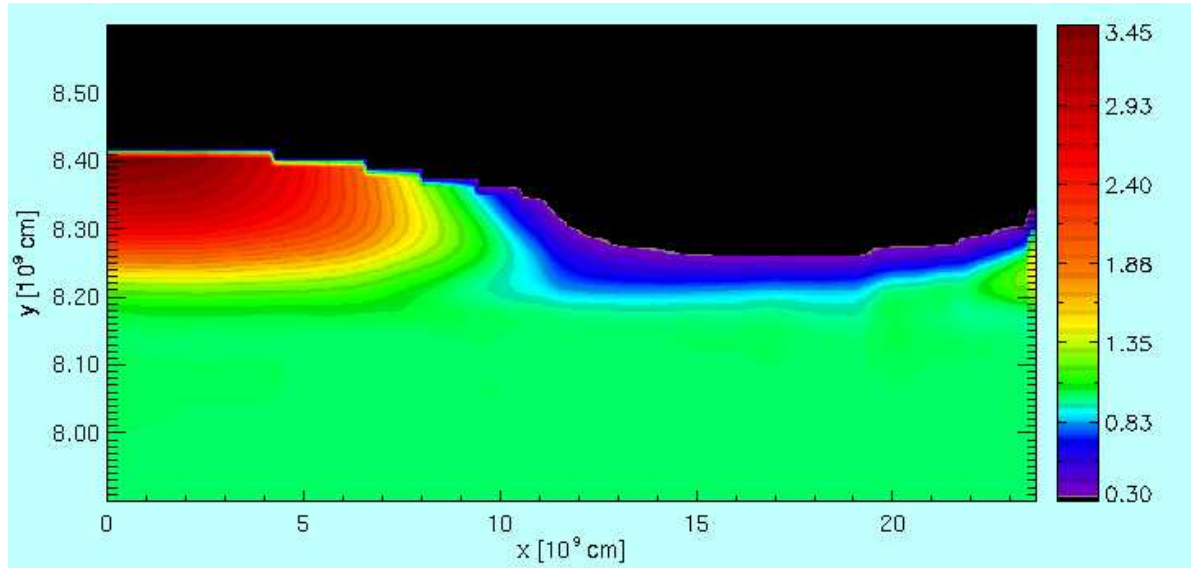


Fig. 2.— The quantity f_p , defined as the ratio of the local pressure to the horizontally averaged pressure at the given value of y , is plotted in the (x, y) plane for Case 1 after the calculation has reached steady state. *Red*: high-pressure regions; *Blue to violet*: low-pressure regions; *Green*: regions where there is no significant local deviation from the mean pressure at the given value of y .

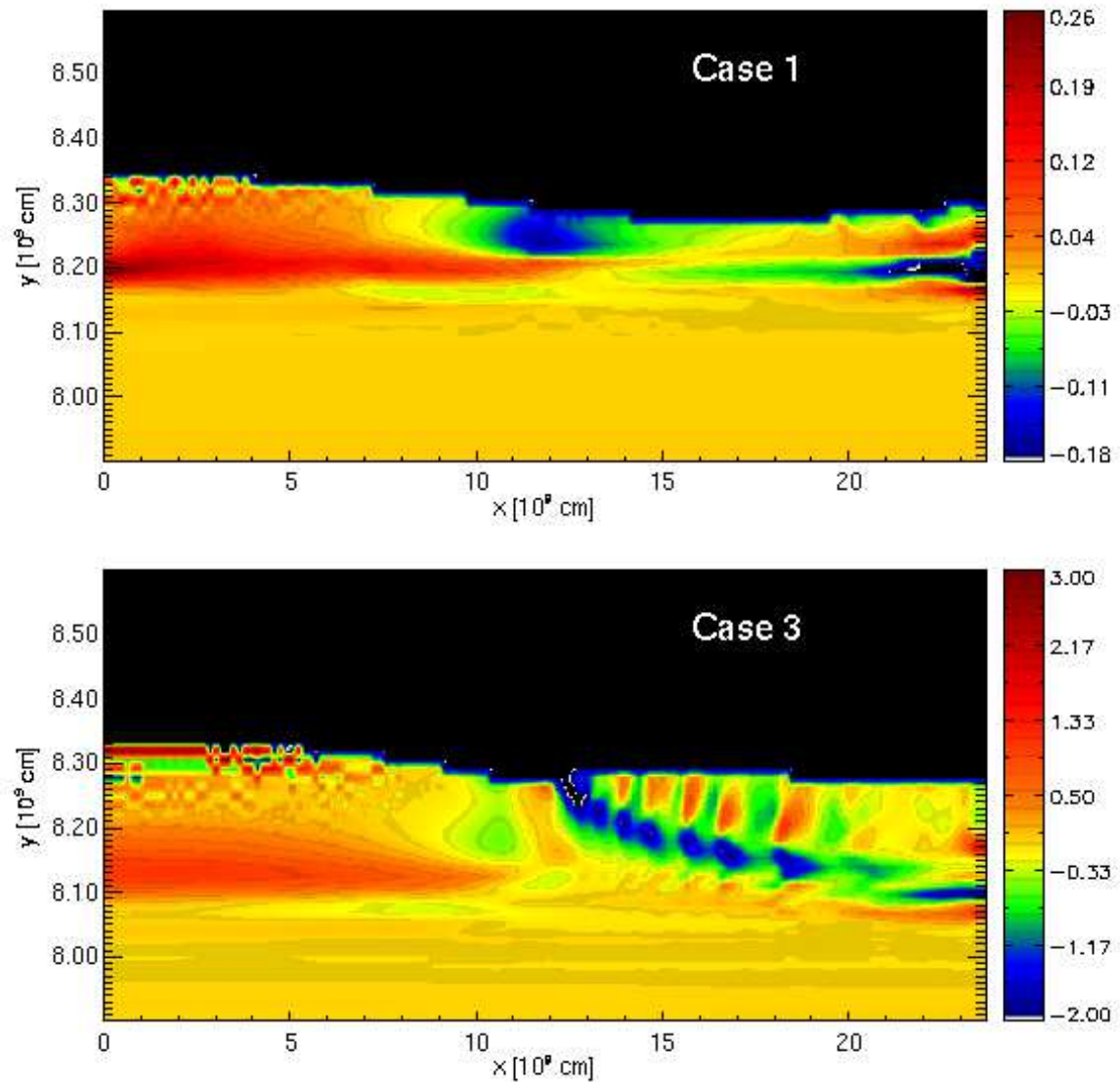


Fig. 3.— The local rate of change of internal energy per unit volume caused by radiation transfer (right-hand side of eq. 4) when the model has reached steady state. Colors represent regions in the (x, y) plane which are strongly heated (brown to red) and which are strongly cooled (blue).

Upper panel: Case 1; *lower panel:* Case 3.

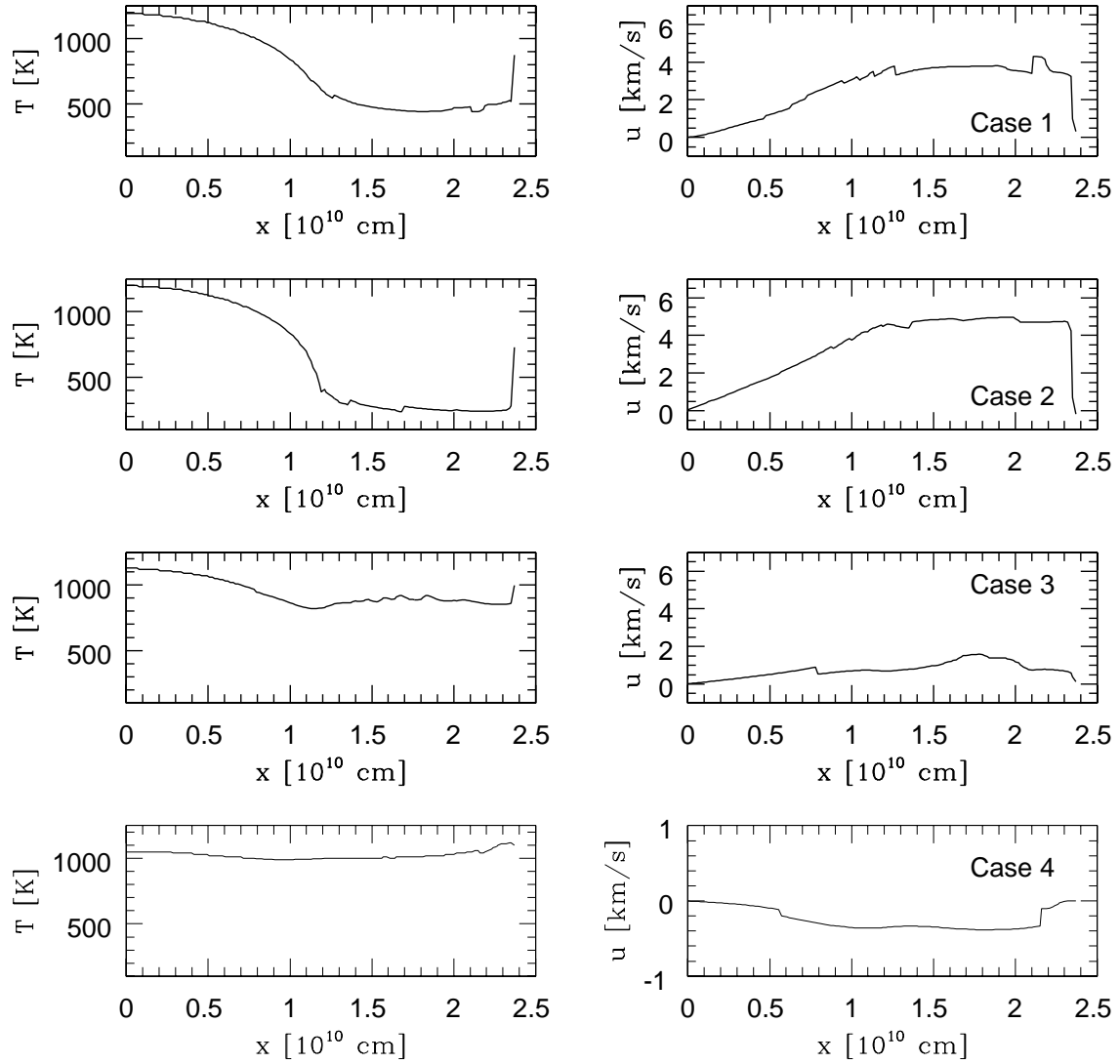


Fig. 4.– The left frames give the temperature as a function of x at the photosphere for the steady-state model. The right frames give the velocity in the x -direction as a function of x , also at the photosphere. *Top to bottom:* Cases 1, 2, 3, and 4.

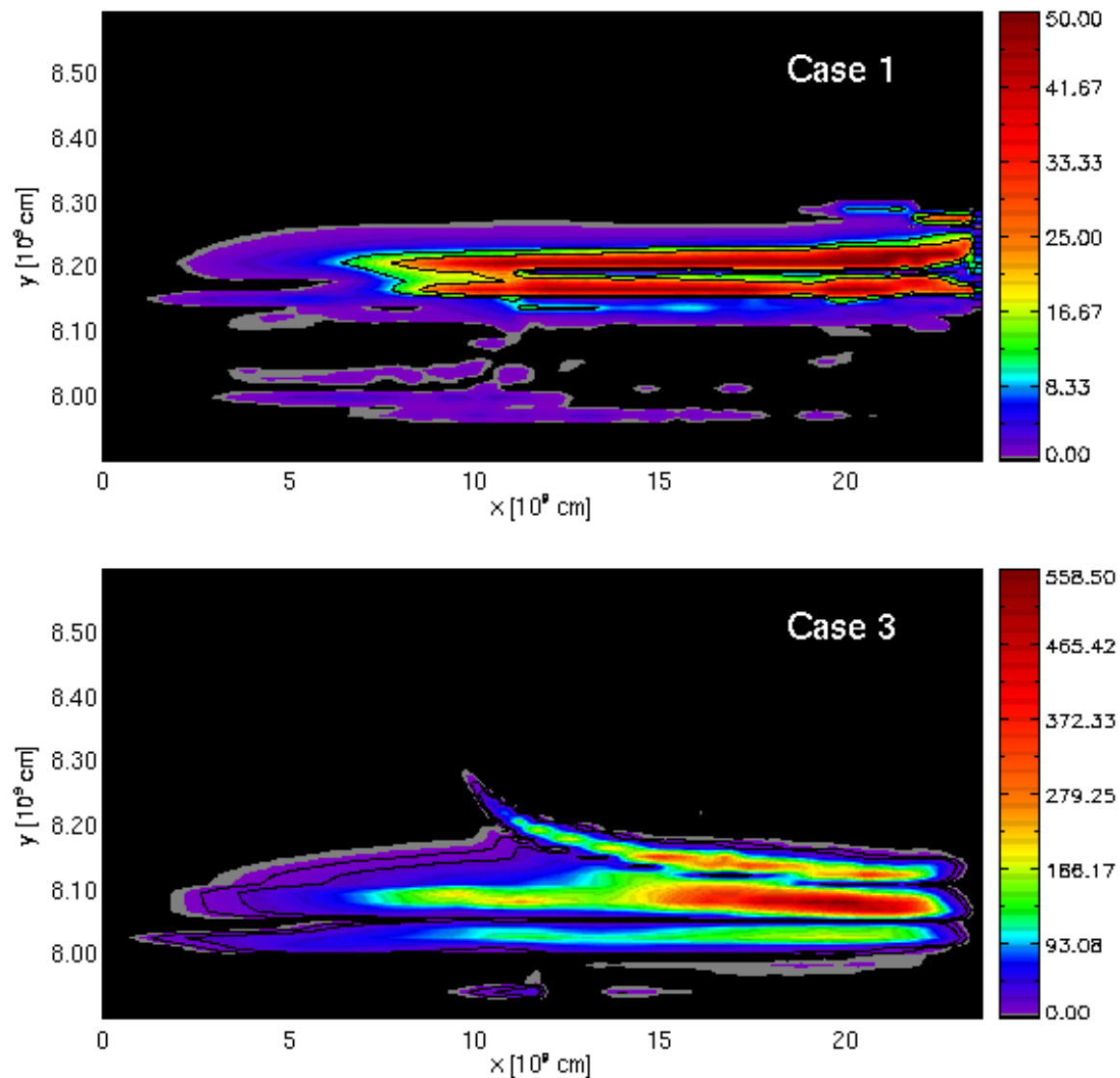


Fig. 5.— The local rate of viscous heating is plotted in the (x, y) plane. *Upper panel:* Case 1; *lower panel:* Case 3.

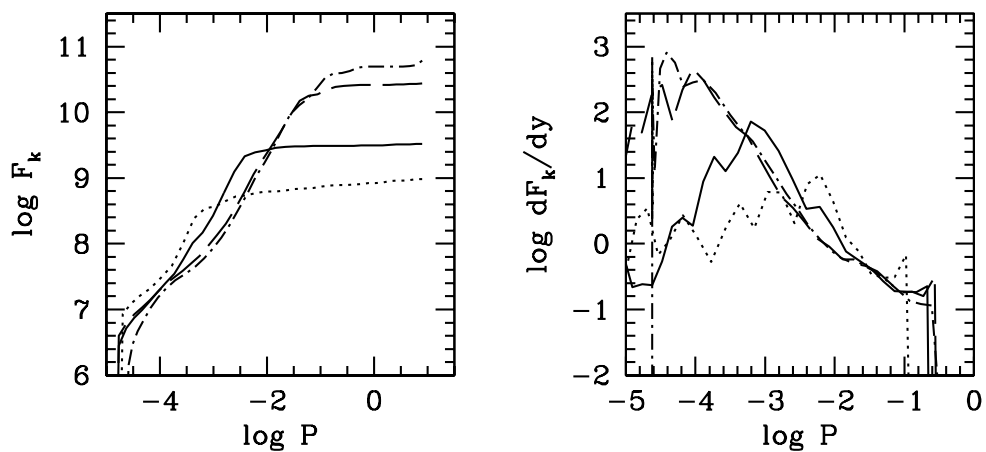


Fig. 6.— *Left frame:* The quantity $\alpha^{-1}F_k$ is plotted, where α is the viscosity parameter and F_k is the rate of viscous dissipation per unit area, integrated downwards to the level where the pressure is P . *Solid line:* Case 1; *dotted line:* Case 2; *dashed line:* Case 3; *dash-dotted line:* Case 4. *Right frame:* the derivative of the function plotted in the left frame.

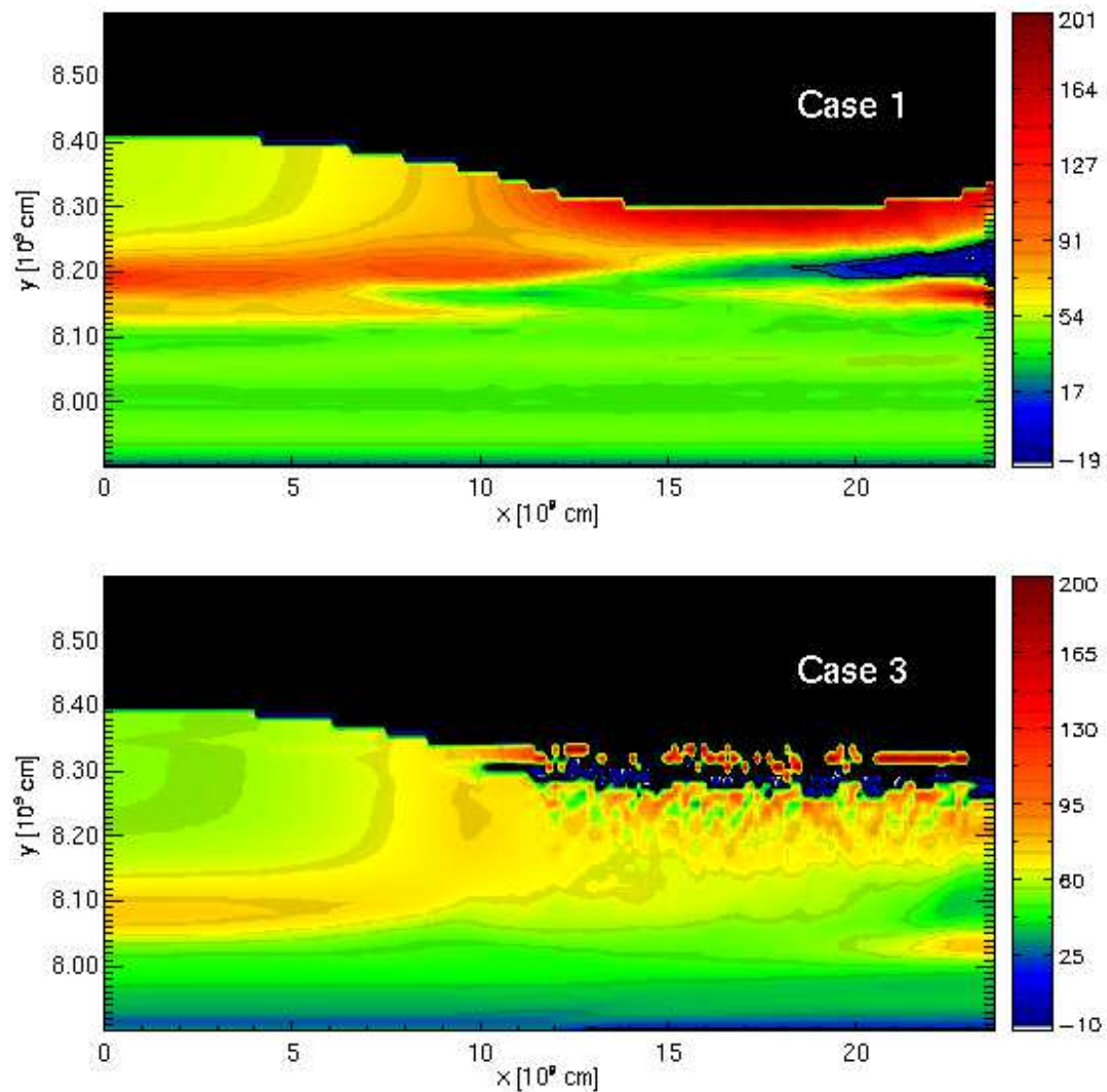


Fig. 7.— The normalized squared Brunt-Väisälä frequency N_n^2 is plotted in the (x, y) plane.
Upper panel: Case 1; *lower panel:* Case 3.